ADVANCED OPTICAL MATERIALS
www.advopticalmat.de

Effects of Varying Deposition Rates of a Carbazole and Triazine Derivative on Its Tunable Emission and Charge-Transporting Properties Beneficial for Efficient Red Electroluminescent Devices

Melika Ghasemi, Joseph Cameron, Woon K. Lin,* Dmytro Volyniuk, Peter J. Skabara, Juozas V. Grazulevicius,* and Gjergji Sini**

The discovery of tunable emission and charge-transporting properties via varying deposition rates of a new derivative of carbazole and triazine is a novel and intriguing aspect of this research, leading to a shortened electroluminescence lifetime in red organic light-emitting diodes. Well-balanced hole and electron transport, along with efficient thermally activated delayed fluorescence (TADF) with an average lifetime of 101 ns in thin films of 9,9'-bis (4,6-diphenyl-1,3,5-triazin-2-yl)-9H,9'H-2,2'-bicarbazole (2Cz2TAZ), is demonstrated. These properties of 2Cz2TAZ support the rapid harvesting of normally long-lived triplet states. This results in reduced efficiency roll-off in organic light-emitting diodes using emitters that exhibit TADF and phosphorescence, when 2Cz2TAZ is employed as the host, compared to a reference device with a conventional host. A maximum external quantum efficiency of 26.2% is achieved for devices using 2Cz2TAZ as the host. Replacing the conventional host with 2Cz2TAZ in the same device structure decreases the average electroluminescence lifetime from 249.6 to 10.7 µs. Balanced hole and electron mobility values exceeding 1×10^{-4} cm^2 Vs^{-1} and the short TADF lifetime support fast electroluminescence. Theoretical and experimental approaches are employed to investigate the tunable electronic properties of the *trans* and *cis* conformers of 2Cz2TAZ.

1. Introduction

Since the invention of organic light-emitting diodes (OLEDs) in 1987 by C. W. Tang and S. A. Van Slyke, considerable advances have been realised through intensive research toward the achievement of high efficiency in solid-state lighting devices and displays.[1] These efforts have been motivated by the unique merits of OLEDs, including flexibility, lightness, stability, high efficiency, low power consumption, high contrast ratio, environmental friendliness, and cost effectiveness.[1–3] The efficiency of OLEDs depends on the factors such as photoluminescence quantum yield (PLQY), internal quantum efficiency (IQE), transport and recombination of electrons and holes.[4] Unlike the 1st generation of OLEDs, in which only singlet excitons are harvested, the 2nd and 3rd generations simultaneously utilize both singlet (maximum of 25%) and triplet (maximum of 75%) excitons.[5] Achievement of the theoretical internal quantum efficiency (IQE) of 100% of OLEDs is possible through intersystem crossing (ISC) in the case of room temperature phosphorescence (RTP), and reverse intersystem crossing (RISC) in the case of thermally activated delayed fluorescence (TADF).[6–8] Due to the involvement of triplet excited states in TADF, phenomena such as triplet-triplet annihilation (TTA), concentration quenching, and triplet-polaron quenching (TPQ) can

M. Ghasemi, D. Volyniuk, J. V. Grazulevicius
Department of Polymer Chemistry and Technology
Kaunas University of Technology
K. Barsausko str. 59, Kaunas LT-51423, Lithuania
E-mail: juozas.grazulevicius@ktu.lt

The ORCID identification number(s) for the author(s) of this article can be found under https://doi.org/10.1002/adom.202501829

DOI: 10.1002/adom.202501829

J. Cameron, P. J. Skabara
School of Chemistry
University of Glasgow
Glasgow G12 8QQ, UK
E-mail: joseph.cameron@glasgow.ac.uk

W. K. Lin
Low Dimensional Material Research Centre
Department of Physics
University Malaya
Kuala Lumpur 50603, Malaysia
E-mail: ph7klw76@um.edu.my

G. Sini
Laboratoire de Physicochimie des Polymères et des Interfaces
CY Cergy Paris Université
Cergy-Pontoise Cedex 95031, France
E-mail: gjergji.sini@cyu.fr

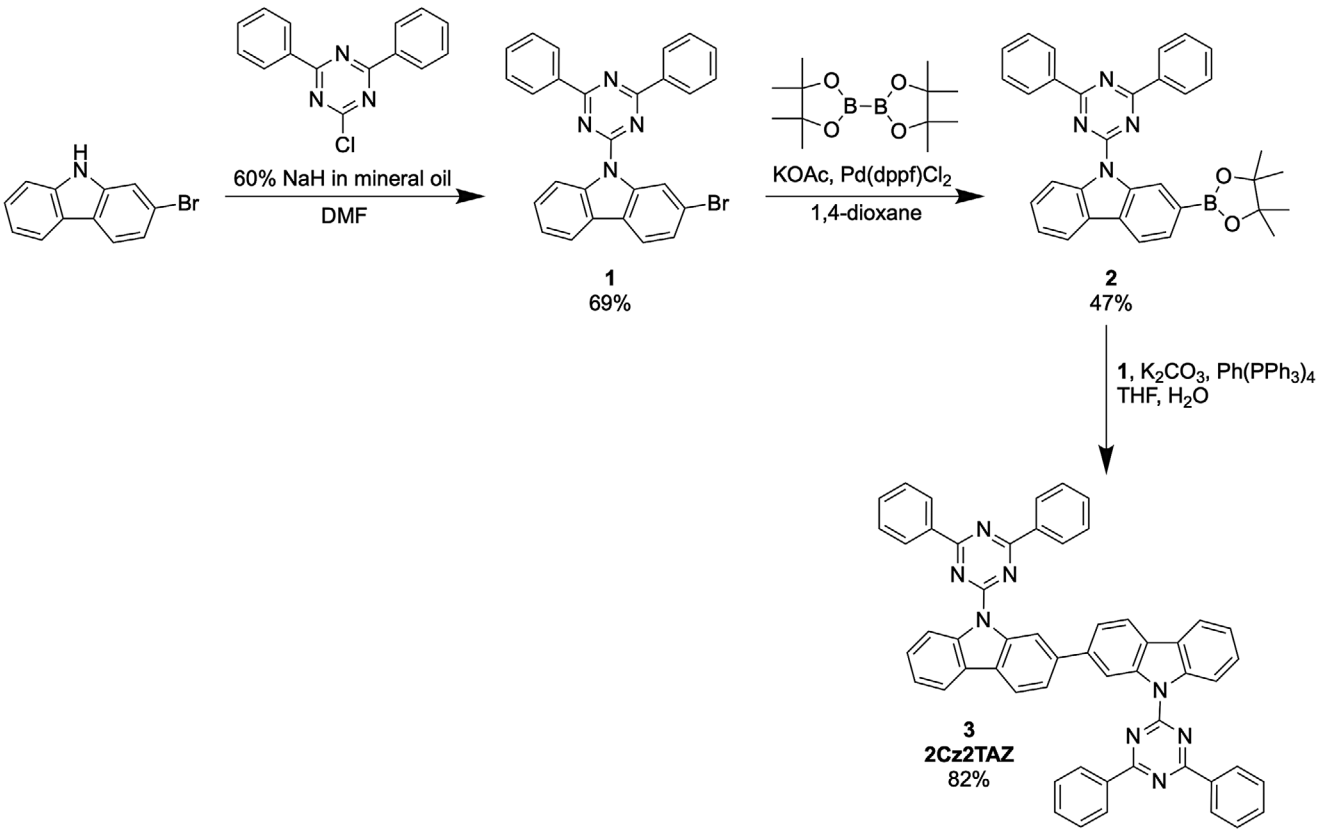

Scheme 1. Synthesis of **2Cz2TAZ**.

significantly impact the emission process.[9] Consequently, devices utilizing non-doped TADF emitters often suffer from poor performance.[10] To mitigate the effects of concentration-induced quenching, TPQ, and TTA, host-guest systems are adapted as the light-emitting layers of OLEDs. In such a case, the hosts serve to reduce the concentration of triplet excitons, leading to improvement in the performance of devices.[11,12]

Organic materials intended as OLED hosts should meet several specific criteria. First, the hosts need to possess a higher triplet energy than the dopants, which promotes efficient energy transfer from the host to the dopant.[13] Secondly, OLED hosts have to have high thermal stability to ensure the formation of durable films.[14] Lastly, the highest occupied molecular orbital (HOMO) and the lowest unoccupied molecular orbital (LUMO) energies of hosts should align with those of the adjacent layers to mitigate charge injection barriers.[14] These criteria are partly met by carbazole-based hosts.[15] Carbazole is one of the most widely employed building blocks of OLED materials owing to its high triplet energy level (^3LE_D of ca. 3.05 eV), excellent hole-transporting abilities ofcarbazole derivatives, their chemical stability, rigid planar molecular structure, etc.[16,17] Electron-donating properties of the carbazole moiety arise from the participation of the electron pair of the nitrogen atom in electron delocalization, inducing negative charges on the carbon atoms.[16,17] However, high hole mobilities of carbazole derivatives can lead to the imbalance of charge carriers in the light-emitting layers (EML) of OLEDs, resulting in poor device efficiencies. To address this issue, electron-accepting building blocks, e.g. triazine, are commonly incorporated in OLED hosts.[18] The electron-accepting property of triazine arises from the equatorial position of the lone electron pairs of the nitrogen atoms, which prevents their participation in the p-conjugation of the carbon atoms, making the nitrogen atoms more effective in stabilization of positive charges or in accepting additional electrons.[19,20] For example, Bao et al. synthesized a bipolar host material containing carbazole as the donor and triazine as the acceptor moieties.[19,20] This compound was used as a host for green phosphorescent OLEDs with the maximum EQE of 15.9%.[21] It is worth of noting that TADF materials are often used as hosts in OLEDs, creating an additional charge-transfer pathway for triplet harvesting that further enhances exciton formation efficiency.[22–25] Qu et al. developed carbazole and triazine derivatives as hosts for a commercial green phosphorescent emitter used in OLEDs with maximum EQEs of 16.5% and 15.4%.[18] In 2024, Zhang et al. developed two bipolar derivatives of benzonitrile and carbazole as hosts for phosphorescent emitter bis(1-phenylisoquinoline)(acetylacetonate)iridium(III) ($Ir(piq)_2(acac)$) in red-emitting OLEDs with maximum EQEs of 16.09% and 25.3%.[26] In another study conducted by Wei et al., a TADF host was used for TADF emitter 2,3,5,6-tetrakis(3,6-diphenylcarbazol-9-yl)-1,4-dicyanobenzene (4CzTPN-Ph) in OLEDs with maximum EQEs of 11.1%.[27] This TADF host showed practically the same performance as it was reported by Adachi et al. for 4CzTPN-Ph based OLEDs with EQE of 11.2% which was observed using a conventional host.[28]

Table 1. Thermal, photoelectrical, and hole-transporting parameters of **2Cz2TAZ**.

Parameters	Sample	2Cz2TAZ
Thermal parameters		
[a] T_m (°C)	Powder	449
[b] T_g (°C)		–
[c] T_{cr} (°C)		411
[d] $T_{d\text{-}5\,\%}$ (°C)		461
Photoelectron emission spectroscopy		
[e] IE_{ups}	Film	5.50
[f] Eg^{opt}		3.17
[e] EA		2.33
Time of flight study		
[g] $\mu_{h/e}$ ($cm^2\ Vs^{-1}$)	LR film	$4.1 \times 10^{-5}/1 \times 10^{-4}$
$\mu_{0h/e}$ ($cm^2\ Vs^{-1}$)		$3.1 \times 10^{-7}/1.4 \times 10^{-7}$
$\beta_{h/e}$ (cm/V)		$4.5 \times 10^{-3}/6 \times 10^{-3}$
[g] $\mu_{h/e}$ ($cm^2\ Vs^{-1}$)	HR film	$3.1 \times 10^{-5}/2.1 \times 10^{-4}$
$\mu_{0h/e}$ ($cm^2\ Vs^{-1}$)		$6 \times 10^{-8}/7.4 \times 10^{-8}$
$\beta_{h/e}$ (cm/V)		$5.8 \times 10^{-3}/7.2 \times 10^{-3}$
Photophysical parameters		
λ_{max}^{PL} (nm)	Toluene:	438/443/456
[h] τ_{avg}, (ns)	aggregate-containing/aggregate-reduced/aggregate-free	12.13/–/3.72
PLQY (%)		4.27/2.91/2.25
λ_{max}^{PL} (nm)	THF:	440/475/479
[h] τ_{avg}, (ns)	aggregate-containing/aggregate-reduced/aggregate-free	12.96/–/5.93
PLQY (%)		5.94/2.81/1.51
λ_{max}^{PL} (nm)	Film	503
[h] τ_{avg}, (ns)		101
PLQY (%)		2.37
[i] E_S (eV)		2.97
[i] E_T (eV)		2.38
ΔE_{ST} (eV)		0.59

[a] Melting temperature (T_m). [b] Glass transition temperature (T_g) (scan rate (10 °C min^{-1}), N_2 atmosphere). [c] Crystallization temperature (T_{cr}) (scan rate (10 °C min^{-1}), N_2 atmosphere). [d] 5 % weight loss temperature ($T_{d\text{-}5\,\%}$, 5% weight loss) (scan rate (20 °C min^{-1}), N_2 atmosphere). [e] Ionization energy (IE_{UPS}). [f] Optical bandgap was obtained from the onset of the low energy absorption spectra via the equation $E_g^{opt} = 1239.84/\lambda_{onset}$. [g] The value of hole mobility was obtained at the electric field of 1×10^6 V cm^{-1}. [h] Average emission lifetimes calculated as shown in Tables S2 and S3 (Supporting Information); [i] Singlet and triplet energy values were estimated from the extrapolation of the high-energy edges of fluorescence and phosphorescence spectra recorded at 77 K.

Taking into account the above-expressed challenges, compound 9,9′-bis(4,6-diphenyl-1,3,5-triazin-2-yl)-9H,9'H-2,2′-bicarbazole (**2Cz2TAZ**) with carbazole and triazine moieties was developed and synthesized. The flat geometry of TADF materials plays a crucial role in facilitating efficient charge transfer and exciton formation.[24] Its planar structure ensures a high degree of orbital overlap between the highest occupied molecular orbital (HOMO) and the lowest unoccupied molecular orbital (LUMO), promoting rapid ISC and RISC processes.[29]

However, when considering the geometry of molecules used for OLED emissive layers, the properties of conformers should also be taken into account. For example, phenothiazine, a popular donor unit used in the design of emissive materials, can exist either in the quasi-equatorial or quasi-axial conformations.[30] As a result, the nature of the emission can change, from TADF to room temperature phosphorescence.[19] The emission of such compounds is often sensitive to mechanical stimulus or solvent vapor treatment.[31,32] Such studies have not yet been extended to host materials, where conformer control may influence exciton dynamics and charge transport in the emissive layer.

The photophysical, thermal, photoelectrical, charge transport, electrooptical, and electroluminescent properties of **2Cz2TAZ** were thoroughly investigated using a combination of theoretical and experimental approaches to examine the complex photophysics of this material and determine its suitability as host or emitter in the emissive layers in OLEDs, including quantum well-based OLED architectures. The fabricated OLEDs exhibited red EL with lifetimes in the microseconds range. OLEDs with the emitting layer of **2Cz2TAZ** and $Ir(piq)_2(acac)$ showed a turn-on voltage of 3.1 V and maximum EQE of 26.2%. The characteristics of devices based on **2Cz2TAZ** were compared with those of the reference devices containing conventional host 3,3′-di(9H-carbazol-9-yl)-1,1′-biphenyl (mCBP). Using **2Cz2TAZ** instead of mCBP in devices exploiting the same device structure resulted in

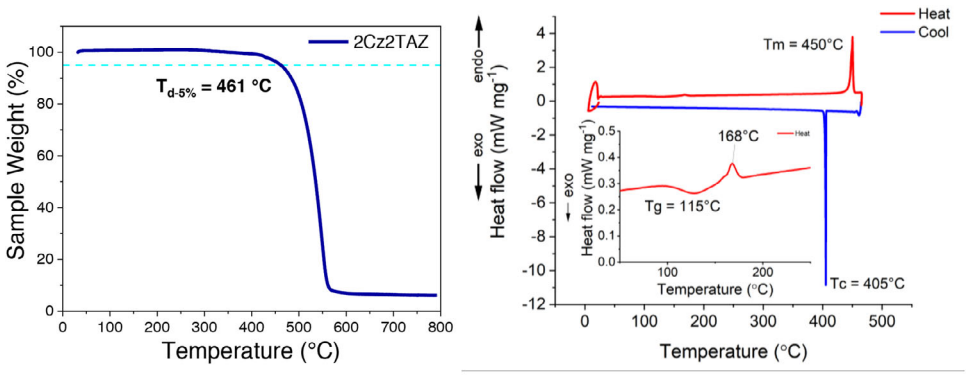

(a) (b)

Figure 1. TGA a) and DSC b) plots of powders of **2Cz2TAZ**. Inset of the DSC plot shows the heating cycle over a lower heat flow range, with glass transition and phase transition peak visible.

shortened average electroluminescence lifetimes of 10.7 µs versus 249.6 µs, and in improved efficiency roll-off.

2. Results and Discussion

2.1. Synthesis

A nucleophilic substitution reaction with 2-bromocarbazole and 2-chloro-4,6-diphenyltriazine was carried out to give compound **1** in 69% yield. A Miyaura borylation reaction with bis(pinacolato)diboron formed the boronic ester, **2**, in 47% yield (**Scheme 1**). This allowed both compounds **1** and **2** to be used in a Suzuki cross-coupling reaction to give target compound **3**, **2Cz-TAZ**, in high yield (82%). Due to the low solubility of **2Cz2TAZ** compared to the starting materials, it could be easily purified without the need for column chromatography.

2.2. Thermal Analysis

To unclose the potential of **2Cz2TAZ** for solid-state applications, the thermal characteristics of **2Cz2TAZ** were examined by employing differential scanning calorimetry (DSC) and thermogravimetric analysis (TGA) under a nitrogen atmosphere. The summary of the thermal properties of the compound is presented in Table 1. The TGA curve revealed remarkably high 5% weight loss temperature of 461 °C which surpasses those reported for molecules containing single carbazole and one triazine moieties (**Figure 1a**). The complete weight loss in the single stage indicates that this temperature shows the onset of sublimation rather than thermal degradation. The first heating scan of the DSC for **2Cz2TAZ** revealed a sharp endothermic peak at 450 °C, corresponding to the melting point (T_m) (Figure 1b). The cooling scan exhibited a very sharp exothermic peak (T_c) at 405 °C caused by the crystallization. A glass transition temperature (T_g) could be observed at 115°C during the heatingscan of the sample, although the reverse transition is not visible upon cooling, above 0 °C. There is also a small endothermic peak at 168°C, which is assigned to a phase transition in the solid material.

2.3. Geometrical, Electronic, and Redox Properties

Density functional theory (DFT) simulations were conducted to investigate the molecular structures of the compound. **Figure 2a** illustrates the relationship between the carbazole-carbazole dihedral angle and the potential energy of **2Cz2TAZ**, suggesting the potential presence of *cis* and *trans* conformers simultaneously. The *cis* and *trans* **2Cz2TAZ** conformers are shown in Figure 2b. The carbazole-carbazole dihedrals are of 35.6° and 29.1° for *trans* and *cis* conformers, respectively. Several local minima are observed with respect to the carbazole-carbazole dihedral angle, with the *trans* conformer having the lowest energy at a carbazole-carbazole dihedral angle of -150°, and the *cis* conformer with a dihedral angle of ≈30° being 34 meV (3.3 kcal mol^{-1}) higher in energy than the *trans*-conformer. Both the conformers are confined within potential wells with a height of at least 0.15 eV (3.5 kcal mol^{-1}, Figure 2a), indicating relatively low potential barriers for torsional rotations between the two carbazole fragments.

As for dihedral angle between the carbazole and triazine units, the results indicate small dihedral angles of 10.5° and 18.0° for *trans* and *cis* conformers, respectively, which is the result of competition between at least two effects: i) the establishment of hydrogen bonds of roughly 2.22 Å between the lone-pairs on the TAZ fragments, and the adjacent C—H bonds of the carbazoles, and ii) the repulsion between the above-mentioned H atoms and the H atoms of the phenyl groups linked to the TAZ fragment (see Figure 2c). Our test calculations indicate that in the absence of the phenyl groups, practically perfectly planar geometry can be achieved with donor-acceptor dihedrals of 2°–4°.

The torsional angle between the donor and acceptor units is more constrained in the *trans* isomer, with a potential barrier of ca. 0.4 eV (9.2 kcal mol^{-1}), which seems coherent with the presence of two strong hydrogen bonds. Finally, the TAZ-Ph dihedral angles inside the acceptor unit are very small, ranging from 6° to 9°.

From the above-disclosed structural parameters, we highlight the nearly planar (flat) layout of the donor and acceptor moieties. Moreover, in view of the rigidity and of the flatness of the donor and acceptor units, strong π-π stacking interactions can be suspected for this compound. Indeed, a molecular dynamic simulation in toluene has confirmed the presence of

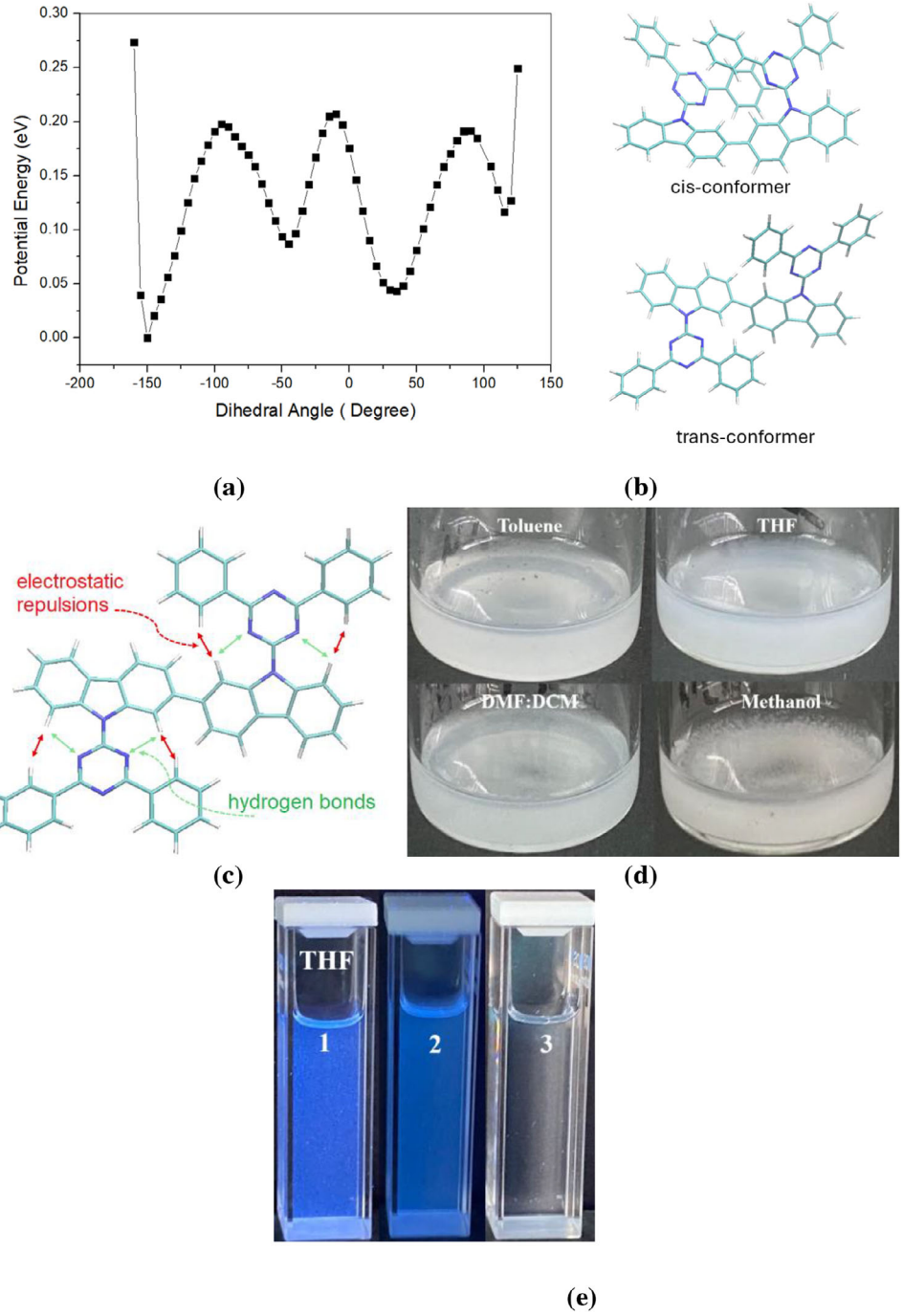

Figure 2. a) Potential energy profile as a function of dihedral angle between two carbazole moieties. The energy minima correspond to the *cis* (≈30°) and *trans* (≈−150°) conformers. b) The *cis* and *trans* conformers of **2Cz2TAZ**.c) Geometry of the model compound **2Cz2TAZ** d) View of the solutions after sonification and heating for 30 min, still indicating the presence of aggregates. e) View of the THF solutions under UV excitation (1 is freshly prepared THF solution; 2 is THF solution after sonification and heating for 30 min; and 3 is aggregate-free THF solution (stabilized overnight)).

π-π stacked **2Cz2TAZ** (Figure S1, Supporting Information), which significantly impacts the solubility and the optical properties of the corresponding solutions. These results find support from the pictures shown in Figure 2d,e, indicating the presence of undissolved **2Cz2TAZ** powder in different solvents after 30 min of sonication and heating.

The frontier orbitals of *cis*- and *trans*-**2Cz2TAZ** are shown in **Figure** 3a, with the hole and electron natural transition orbitals shown in Figure 3b. The distributions of HOMO and of LUMO are strictly limited to the donor and acceptor moieties, respectively. This result i) is counterintuitive, given that the almost "flat" donor-acceptor geometry (dihedrals ranging from 10° – 18°)

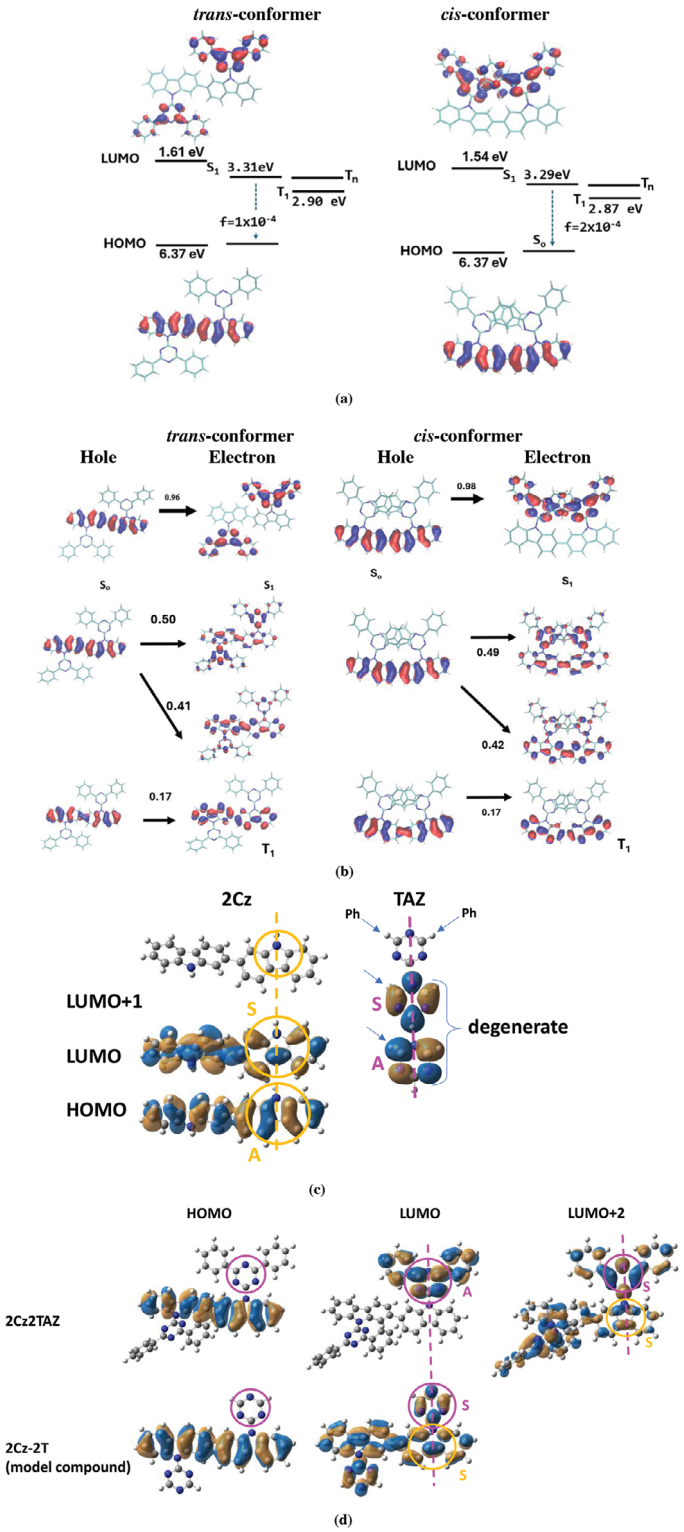

Figure 3. a) Frontier orbitals, lowest singlet and triplet vertical transition energies and singlet-triplet splitting and b) hole and electrons of the lowest vertical transition for S_o-> S_1 and T_o->T_1 for *trans*-**2Cz2TAZ** and *cis*-**2Cz2TAZ**. c) Frontier orbitals of **2Cz** along with LUMO and LUMO+1 (degenerate) of **TAZ**. The symmetry properties for the **TAZ** orbitals are shown with regard to the plane normal to the molecule, as highlighted by the orange and pink dashed lines (S stands for symmetric, and A for antisymmetric). A similar description of the symmetry properties for the encircled parts of the HOMO and LUMO of the dicarbazole fragment are shown with respect to the orange dashed line located at the carbazole-TAZ linking position. d) Frontier orbitals of **2Cz2TAZ** and the model compound **2Cz-2T**. The LUMO+2 of **2Cz2TAZ** is also shown. In the case of the virtual orbitals, the local symmetric and antisymmetric properties at the 2Cz and TAZ groups (encircled) are indicated with respect to the plane normal to the figure and visualized by the pink dashed line.

should promote good pi-conjugation between the two groups, and ii) indicates that, in addition to the near-orthogonal D-A geometry targeted for HOMO-LUMO space-separation, other properties seem to allow for the HOMO-LUMO separation. Indeed, recently Kuila et al. demonstrated examples of rigid molecules of fused indolocarbazole-phthalimide derivatives which underwent intramolecular charge transfer and exhibited TADF.[30]

In order to understand the counterintuitive behavior in the case of **2Cz2TAZ**, in Figure 3c we show a selection of molecular orbitals for the isolated di-carbazole moiety and TAZ. In this figure we highlight the following: i) the isolated TAZ fragment exhibits a doubly degenerate LUMO level, one symmetric- and the other antisymmetric with respect to one N...C axis highlighted by the pink dashed line. The similar symmetry characterizations are provided for the encircled part of the isolated dicarbazole moiety, indicating locally-symmetric- and locally antisymmetric properties for the encircled parts of LUMO and HOMO of dicarbazole, respectively. ii) The wavefunction coefficients at the Ph···TAZ linking positions (highlighted by the blue arrows) are larger for the antisymmetric LUMO than for the symmetric one, suggesting stronger TAZ···Ph interactions by means of the antisymmetric orbital, hence the antisymmetric property for the LUMO(TAZ-Ph). This electronic structure results in zero overlap between the encircled part of LUMO(2Cz) (locally-symmetric) and the antisymmetric LUMO(TAZ-Ph) in **2Cz2TAZ**, hence the strict localization of the LUMO(**2Cz2TAZ**) on the acceptor TAZ-Ph group(s) only. This analysis is corroborated by 2 additional results: i) the LUMO+2 of **2Cz2TAZ** is distributed over the entire molecular skeleton, due to the interaction of the locally-symmetric LUMO(2Cz) (included inside the orange circle) with the symmetric LUMO+1(TAZ-Ph), see Figure 3d. ii) Removing the phenyl groups from **2Cz2TAZ** gives rise to a model compound reported hereafter as **2Cz-2T** (Figure 3c), allowing restoration of the degeneracy of LUMO(TAZ) and LUMO+1(TAZ). As expected, our test calculations on this model compound results in LUMO(**2Cz-2T**) distribution over the entire molecular skeleton (Figure 3c), in turn stemming from the interaction between the locally-symmetric LUMO(2Cz) with the symmetric LUMO(TAZ-Ph).

As equivalent dihedral angles in the *cis*- and *trans* isomers are of similar magnitude, it is expected that the calculated energy levels are similar. The HOMO energies determined for both conformers have the similar energies of 6.37 eV, while the LUMO levels are slightly shallower, with energies of 1.54 and 1.61 eV for the *cis* and *trans* conformers, respectively.

We focus now on the experimental characterization of the redox properties of **2Cz2TAZ**. Unfortunately, the solubility of **2Cz2TAZ** was not sufficient for cyclic voltammetry measurements. Ultraviolet photoelectron emission spectroscopy (UPS) experiment performed in air was employed for the estimation of the ionization energy (IE_{UPS}) of the thermally evaporated film of **2Cz2TAZ**. The IE_{UPS} value was estimated by extrapolating the linear part of the UPS spectra to the horizontal axis. It was found to be of 5.50 eV (Table 1; and Figure S2, Supporting Information). The obtained value aligns with those of the derivatives of carbazole and triazine.[19] This value is thus favorable for the injection of holes, making this compound a good candidate for hole-transporting layers of organic electronic devices. The electron affinity (EA) was calculated by means of the formula $EA = IE_{UPS} - Eg^{opt}$. A Eg^{opt} value of 3.17 eV was calculated using the optical bandgap, obtained from the low energy band of the absorption spectrum of the solid sample (**Figure 4**). By injecting this last value and the IE_{UPS} value of 5.50 eV (Table S4, Supporting Information) in the above formula, we deduce an EA_{PE} value of 2.33 eV. This result predicts suitable electron injection performances for **2Cz2TAZ** in OLEDs (Table 1).

2.4. Optical Absorption Properties

Having determined that **2Cz2TAZ** has the appropriate thermal stability and energy levels for use in the emissive layer of an OLED, it was important to determine the nature of its absorption and emission states. In this section, we analyse the nature of the lowest-energy optical absorption band, and establish the necessary link with the nature of the vertical excited states determined by calculations. To this aim, in Figure 4 we show the experimental absorption spectra of the solution of **2Cz2TAZ** in toluene and of thin film, along with the theoretical absorption spectrum. The comparison of the normalized experimental and theoretical absorption spectra of the *cis* and *trans* conformers of **2Cz2TAZ** in toluene (Figure 4a) indicates that the excited states of the *cis* conformer tend to be slightly lower energy, but the three spectra practically overlap. The theoretical results are also illustrated in Figure S3a,b (Supporting Information) showing energy diagrams corresponding to the vertical transitions up to S5 or S6 for *trans* and *cis* conformers of **2Cz2TAZ**, respectively.

These results indicate that the four lowest singlet states (S_1-S_4) are of pure charge transfer (CT) character for both conformers, with practically zero oscillator strength. This observation is in line with the total space-localization of the HOMO and LUMO on the donor and acceptor moieties, respectively (Figure 3a; Tables S4 and S5, Supporting Information). The first absorbing (non-dark) excitations for the *trans* conformer correspond to S5 and S7, with oscillator strengths of 0.39 and 0.79, respectively, both exhibiting mixed local-donor and CT characters. A similar description is valid for the *cis* conformer (Tables S4 and S5, Supporting Information). Figure 4 indicates that the lowest-energy absorption band corresponds to several optical transitions, with the lowest-energy one being the S0→S5, S7, S11 for the *trans* conformer, and S0→ S5, S9, S10, S11 for the *cis* conformer. As for the triplet states, the lowest one is dominantly of LE character plus a little CT character, whereas T_2-T_4 are pure CT transitions.

The impact of aggregation on the absorption spectra of **2Cz2TAZ** can be estimated from Figure 4a, in addition to the effect of aggregation visible in Figure 2d,e. Compared to the absorption spectrum of the toluene solution, the optical absorption profile of aggregates is redshifted and broadened, indicating strong intermolecular interactions. The absorption spectrum of the film of **2Cz2TAZ** (Figure 4b) is very similar to that of the aggregate-containing toluene solution (Figure 4a). Our theoretical results obtained by calculating example dimers of **2Cz2TAZ** are in line with the experimental findings. The energy diagrams of the vertical absorption transitions of these dimers are shown in Figure S4 (Supporting Information), indeed indicating some redshifts of the excited state energies as compared to those of the isolated compound.

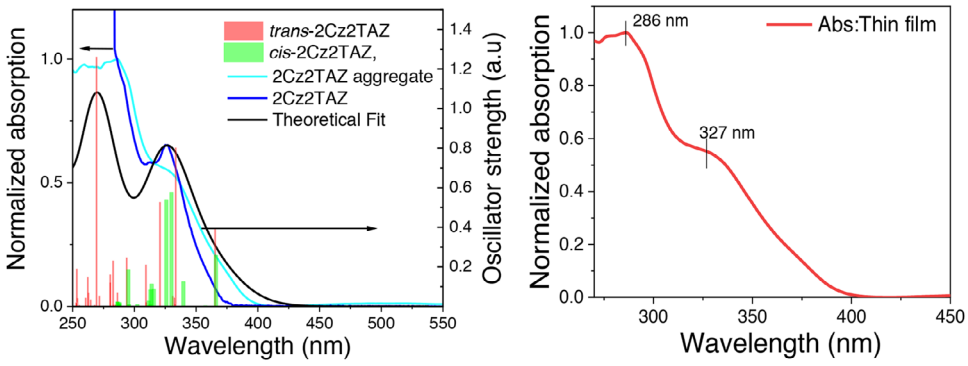

(a) (b)

Figure 4. a) Absorption spectra of toluene solutions of **2Cz2TAZ** recorded after 30 min of sonification in the absence and the presence of aggregates. The theoretical results showing several excited states and their oscillator strengths for the *trans* and *cis* conformations of **2Cz2TAZ** are also shown. The theoretical energies of the excited states are redshifted by 0.2 eV to fit the maxima of the experimental bands. The theoretical fit is based on vertical excitation with gaussian broadening of 0.2 eV b) Absorption spectrum of the vacuum-deposited film of **2Cz2TAZ**.

2.5. Optical Emission Properties

Full characterization of the photoluminescent properties was necessary to determine the suitability of **2Cz2TAZ** as an emissive material. The photoluminescence (PL) spectra of the **2Cz2TAZ** solutions in toluene, THF, and DMSO recorded at RT, along with the PL and phosphorescence spectra of the film and of the THF solution at 77 K are shown in **Figure** 5a–c. The emission of the vacuum-deposited film of **2Cz2TAZ** exhibits a greenish-blue color. A large Stokes shift of ca. 179 nm is found, suggesting a considerable change in molecular geometry from the ground state to the excited state structure, as discussed in Annex S1 (Supporting Information). The spectra reveal a Gaussian shape with relatively broad full-width half-maxima (FWHM) of 120 nm. Intriguingly, deceptively low PLQYs were obtained for the aggregate-free solutions of **2Cz2TAZ** in THF and Toluene (Table 1), reaching only of 1.51% and 2.25%, respectively. This strong PL quenching is intriguing, given that the molecule-molecule interactions are absent in aggregate-free solutions, whereas the intramolecular rotations around the D—A bonds are prohibited by the high rotational barriers (Figure 2a). In the following section we try to identify the factor(s) being at the origin of this behavior and of the other emission properties.

2.5.1. The Nature of the Emitting States

Seeking to obtain deeper insights into the photophysics of **2Cz2TAZ**, we first need to identify the emitting state(s). To this aim, we consider two hypotheses: the emission stems i) from the pure CT state S_1, or ii) from the mixed CT-LE state S_5. Both hypotheses raise several questions, given that S1 exhibits practically zero oscillator strength, whereas the emission from S5 would be in violation of Kasha's rule.[33] In order to disentangle this question, we first discuss the presence or absence of the vibronic progression (VP) on the emission spectra. The PL profile of the aggregates-containing solution of **2Cz2TAZ** in toluene at RT exhibits VP (black plot in Figure 5a). Similarly, VP were observed in PL and phosphorescence spectra of THF solutions at 77 K (red and green plots in Figure 5c). Intriguingly, VP was absent in the spectra of aggregate-free toluene solution, and also in PL spectra of RT THF and DMSO solutions, independently from the presence or absence of aggregates (Figure 5a). A detailed discussion about this intriguing observation is given in Annex S2 (Supporting Information).

The presence of the VP in the emission profiles suggests emission from an excited state being of pure local-excitation (LE) character, or from a state bearing a mixed LE and CT character. The theoretical results indicate presence of pure CT character for the excited states S_1-S_4 with practically zero oscillator strengths, and a first absorbing S_5 state of mixed LE+CT character. These characteristics and conclusions remain unchanged after geometry relaxation of the excited states S_1 through S_4 (Table S4b and Annex S1, Supporting Information), whereas some strengthening of the CT character is observed for S5 at the relaxed geometry, but the LE character is still present. (Figure S3c,d and Table S4b, Supporting Information).

These characteristics point to S5 being the emissive state and exclude S1 which lacks LE character. Indeed, time-resolved PL spectra shown in Figure 5c indicate that the green line corresponding to the spectrum of aggregate-free THF solution recorded at 77 K with the delay of 80 µs exhibits clear VP in the region of 400–500 nm. This delayed contribution can only stem from TADF operating through the same excited state as the prompt PL, again indicating that the PL emitting state must contain some LE character, which is compatible with S5 but not with S1.

The energy values of the relaxed S1 and S5 states in conjunction with the observed colors shown in Figure 5e also point to the same conclusion. Indeed, the relaxed energies found for S_1 and S_5, are 2.08 eV (597 nm) and 3.19 eV (389 nm), respectively. However, these calculated values do not include the solvent (medium) relaxation, which is expected to be strong given the pure CT and dominantly CT character of S_1 and S_5, respectively. Consequently, the real S1 and S5 energies are expected to be even smaller. This suggests that the emission from S_1 would appear in the orange-red region, which is at odds with i) the blue-cyan emission colors shown in Figure 5e for the films annealed at different

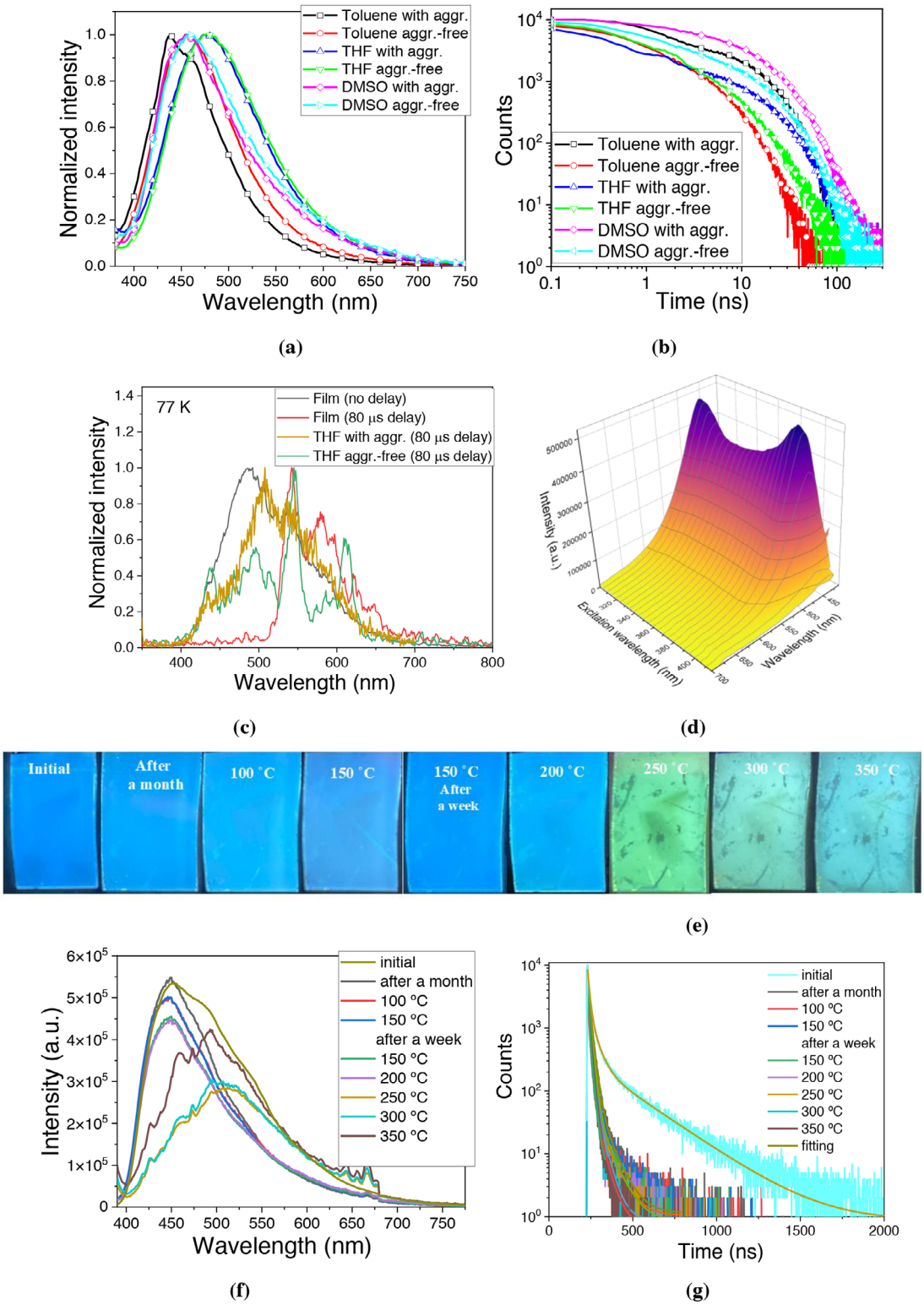

Figure 5. a) PL spectra and b) PL decay curves of aggregates-containing (with aggr.) and aggregates-free (aggr.-free) toluene, THF, and DMSO solutions of **2Cz2TAZ**. c) PL spectrum of the film and phosphorescence spectra of the film and THF solution of **2Cz2TAZ** taken at 77 K. Phosphorescence spectra were recorded using a delay of 0.08 ms after excitation. d) PL spectrum of the film of **2Cz2TAZ** recorded at different excitation wavelengths. e) The film deposited at 3.7 A s^{-1} was selected for the annealing experiment. The sample was annealed with 50 °C increments from 0 to 350 °C for 15 min for each temperature. f,g) PL spectra and decay curves of the films after annealing as indicated in e). The excitation wavelength of 374 nm and the emission wavelengths at maximum PL intensity were selected for recording of PL decays.

temperatures, and ii) with the deep blue emission observed for the THF solution (Figure 2e).

Finally, the hypothesis considering S5 as an emissive state finds strong support from the experimental results shown in Figure 5d: the intensity of PL spectra of the films exhibits a maximum at the excitation energy of 3.18 eV (390 nm), which is close to the S_5 energy level, but drastically drops down very rapidly for excitations of energy. Furthermore, the PL profile of the evaporated films is almost flat when exciting with a wavelength of 410 nm (2.95 eV) and below, which are situated very close to the absorption onset but well above the energy levels of the excited states S_1 and S_2 (2.08 eV), indicating that S_1 (and S_2) is a dark state (Figure 5d).

All in all, we can safely conclude that the presumption that the emission of **2Cz2TAZ** stems from S_1 is incoherent with the ensemble of the experimental and theoretical data. Accordingly, we are led to the conclusion that, in violation with Kasha's rule,[33] the PL of **2Cz2TAZ** in toluene solutions and in the films at RT stems from a radiant high-lying mixed state (such as S_5).

We close this section by highlighting that the deceptively low PLQY of 1.51% and 2.25% of aggregates-free solutions of **2Cz2TAZ** in THF and Toluene (Table 1), respectively, can be traced back to the competition between two deexcitation channels: the anti-Kasha emission from a high-lying excited state such as S_5 (hot TADF), and the IC from S_5 to S_1. The latter state is a dead-end for the excitons, as indicated by the practically zero oscillator strength. It is worth noting that the IC from S_5 down to S_1 is predicted to be quite efficient given the small energy splitting between consecutive states (<0.2 eV, Figure S3a,b, Supporting Information). It can be then tempting to hypothesize that only a small percentage of excitons relax directly from S_5 to S_0, while the majority undergo the IC from S_5 down to the dark state S_1, and subsequently relax non-radiatively to the ground state.

2.5.2. TADF Properties

In the previous section we established that **2Cz2TAZ** cannot be utilized as an efficient emitter because of the very low PLQY. Here we want to evaluate the potential and the efficiency of **2Cz2TAZ** as host material for triplet harvesting through the TADF mechanism.

We turn now our attention to the experimental results. First, the comparison of intensities of PL spectra and PL decay curves recorded in vacuum and in air (Figure S5a,b and Table S2, Supporting Information), disclosed that the emission of the thin film of **2Cz2TAZ** is weakly sensitive to the presence of oxygen. This observation is also supported by the comparison of the emission intensities of air equilibrated and deoxygenated chloroform solutions. It indicated the presence and possible contribution of the triplets to the emission (Figure S5c, Supporting Information), hence contribution from TADF. Additionally, the PL decay curves of the film of **2Cz2TAZ** with the tails reaching 3–5 µs (Figure S5b, Supporting Information) are well fitted by the triple exponential function with the lifetimes of τ_1, τ_2, and τ_3 of 20, 72.6, and 345 ns, respectively (Table S2, Supporting Information). The presence of the delayed fluorescence component, which does not exceed 345 ns, indicates fast TADF. This conclusion is corroborated by the theoretical calculations. Indeed, assuming a reorganization energy of $\lambda = 0.10$ eV for the $T_n \rightarrow S_5$ transitions (where the relevant triplets lie within 0.04 eV below S_5), and using the values of spin-orbit coupling (SOC) from Table S6a (Supporting Information), we apply the semiclassical non-adiabatic Marcus expression:

$$k = \frac{2\pi}{h\sqrt{4\pi\lambda k_B T}} |H_{SOC}|^2 \exp\left[-\frac{(\Delta E + \lambda)^2}{4\lambda k_B T}\right] \quad (1)$$

where H_{SOC} is the SOC matrix element between T_n and S_5, ΔE is the corresponding energy gap. The resulting lifetimes ($\tau = 1/k$) are $\tau_{T13\rightarrow S5} = 75.2$ ns (*trans*-2Cz2TAZ), $\tau_{T12\rightarrow S5} = 695$ ns (*cis*-**2Cz2TAZ**) which both fall below 1 µs.

To confirm this interesting TADF behavior of **2Cz2TAZ**, the PL spectra, PL decay curves and integrated PL intensities of the film were collected over the temperature range from 77 to 300 K (**Figure 6a–c**). The small shift in the emission spectra from 77 to 300 K (Figure 6a) can be attributed to vibrational effects: with the rise of the temperature, high-energy molecular vibrational modes become more populated, causing changes in energy levels and, consequently, alterations in emission spectra.[34] Temperature-dependent intermolecular interactions can further influence the emission spectra.[35–37]

The impact of temperature on the PL lifetime and PL intensity are shown in Figure 6b,c: upon increasing temperature from 77 to 180 K, the emission intensity of the film increases (Figure 6c), and the average PL lifetime increases from 86 to 89 ns (Figure S6 and Table S3, Supporting Information). Both observations are compatible with the presence of TADF in these PL results. As for the PL intensity decrease upon temperature increase from 180 to 300 K (Figure 6c), additional factors may play, such as decreased impact from AIEE, but also to the enhanced propensity to IC within the triplet manifold.

A crucial factor in selecting a host material for TADF OLEDs is the triplet energy level.[2] To experimentally estimate the singlet and the triplet energies of **2Cz2TAZ**, the fluorescence and phosphorescence spectra of the solid-state sample were taken at 77 K (Figure 6d). Using the delay of 20 µs, delayed fluorescence was still observed at 77 K. The singlet (2.97 eV) and triplet (2.38 eV) energies were obtained from the high-energy edges of the fluorescence and phosphorescence spectra Figure 6d. The singlet and triplet energy values are similar to that of well-known host CZ-p-TRZ.[38] The high triplet energy of **2Cz2TAZ** makes it a good candidate as a host for OLED emitters.

Intriguingly, a very large $\Delta E_{S\text{-}T}$ of 0.59 eV can be deduced from the above values, which is incompatible with the fast TADF observed experimentally and calculated theoretically for **2Cz2TAZ**. On the other hand, the theoretical T_1-S_1 energy splitting obtained at the relaxed geometries of the *trans* conformer is 0.17 eV, much smaller than the experimental $\Delta E_{S\text{-}T}$ of 0.59 eV. Aiming at disentangling these dichotomies, we turn our attention to the mechanism of the observed TADF. First, from Figure 5c one can observe that the TADF contribution to the fluorescence (green and brown lines in the PL region between 400–500 nm) and the PL (black line) exhibit identical onset energies, hence involve the same emitting singlet state, meaning the S_5 in the case of *trans* conformer. On the other hand, the phosphorescence spectrum exhibits a clear VP, which is compatible with phosphorescence

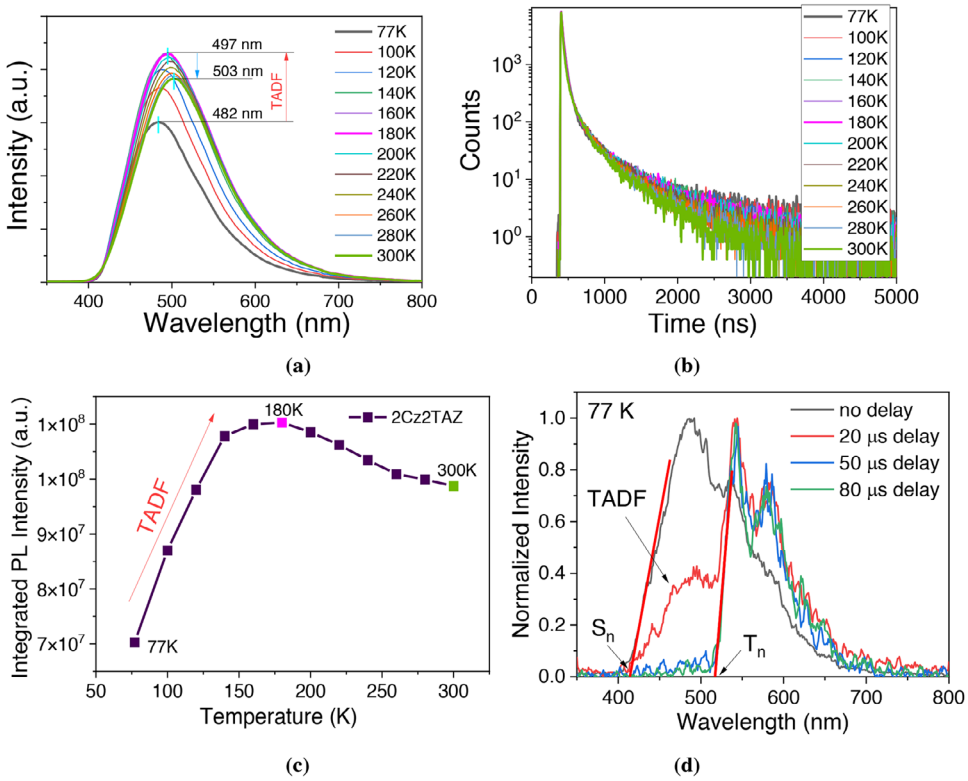

Figure 6. a) PL spectra and (b) PL decay curves recorded at different temperatures. c) Integrated PL intensities as the function of temperature and d) the PL and phosphorescence spectra of the vacuum-deposited film of **2Cz2TAZ** recorded at 77 K. The excitation wavelengths were of λ_{ex} = 330 nm for PL spectra and of λ_{ex} = 374 nm for PL decay curves. For the separation of phosphorescence spectrum from the prompt and delayed fluorescence spectra, different delays were used after excitation.

spectrum stemming from the dominantly LE T_1 state. Accordingly, the experimental $\Delta E_{S\text{-}T}$ should correspond to the energy difference between T_1 and a high-lying singlet excited state, very probably S_5 as discussed in Section 2.5.1.

Admittedly, in view of the high $\Delta E_{S\text{-}T}$ of 0.59 eV found for the film of **2Cz2TAZ**, the direct $T_1 \rightarrow S_5$ rISC as a feeding channel for the observed fast TADF can be excluded. Consequently, we are led to the conclusion that the observed TADF involves one or more high-lying triplet states T_n close to S_5, in competition with the IC from these high-lying triplet states down to T_1.

The presence of this competition between the hot-TADF versus IC can be justified by the large theoretical T_2-T_1 energy splitting of 0.39 eV estimated for the isolated **2Cz2TAZ**, suggesting that the $T_2 \rightarrow T_1$ IC may be importantly suppressed in solutions of **2Cz2TAZ**. Indeed, Figure 5c shows that, after the delay of 80 μs, TADF is still present for the THF solid solution at 77 K in the absence of aggregates (green curve). This TADF signal seems to be reduced in the presence of a small amount of aggregates (brown curve), and is totally suppressed for the solid film of **2Cz2TAZ** (red curve). This evolution can be understood by comparing the excited-state energy diagrams shown in Figure S4a,b,e (Supporting Information). The density of triplet states at the proximity of S_5 and down toward T_1 increases, and the energy gap between T_1-T_2-T_3 decreases importantly when going from monomers (0.39 eV, Figure S3a,b, Supporting Information, isolated **2Cz2TAZ** molecule) to dimers (0.1 and 0.2 eV for T_1-T_2 and T_2-T_3, respectively, Figure S4a,b, Supporting Information), and to the mixture of monomers and dimers (Figure S4e, Supporting Information). This evolution can positively contribute to TADF by increasing the number of rISC channels from the high-energy triplet states and by means of large spin-orbit coupling values (Tables S1 and S2, Supporting Information). Indeed, the contribution of high-lying triplet states to the RISC mechanism can be estimated by considering the SOC matrix elements computed between the singlet and the energetically closest triplet states for both the *trans*- and *cis*-**2Cz2TAZ** conformers, as shown in Table S6a (Supporting Information). The SOC values between some relevant triplets (T_{11}, T_{12}, T_{13}) laying within 0.04 eV below S_5 are $\langle S_5|H_{SOC}|T_{11}\rangle$ = 0.022 cm^{-1} and $\langle S_5|H_{SOC}|T_{12}\rangle$ = 0.050 cm^{-1} for *trans*-**2Cz2TAZ** while $\langle S_5|H_{SOC}|T_{12}\rangle$ = 0.100 cm^{-1} and $\langle S_5|H_{SOC}|T_{13}\rangle$ = 0.230 cm^{-1} for *cis*-**2Cz2TAZ**. These values, in particularly 0.23 cm^{-1} can provide significant strength to facilitate RISC in **2Cz2TAZ**.

As a final point to this discussion, we consider the impact of the aggregation on the efficiency of internal conversion, IC. The largest energy gap inside the triplet manifold decreases upon increasing aggregation from ca. 0.4 eV to less than 0.1 eV, thus suggesting efficient and very competitive IC as compared to the TADF. This competition explains why, after the delay of 80 μs at 77 K, there is still DF in the case of aggregate-free THF solid solution (importantly suppressed IC because of the small density of excited triplet states). However, no DF is observed for the solid film (large density of triplet states, enhancing both TADF and IC efficiencies). Importantly, the presence of the DF after 20 μs in

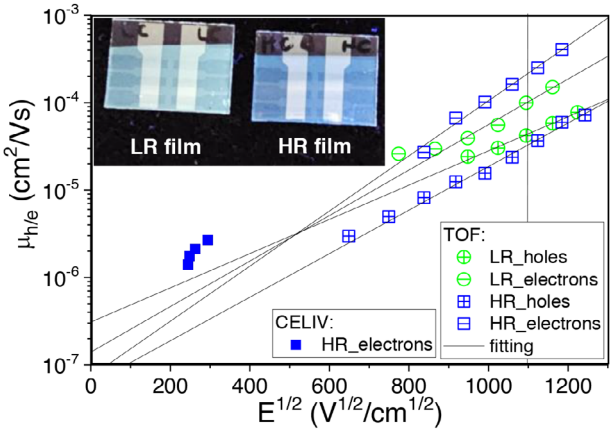

Figure 7. Hole and electron mobility values versus electric field of the LR and HR films of **2Cz2TAZ**. Inset shows a picture of the TOF samples of LR and HR films under UV excitation.

solid film at 77K as opposed to its absence after 80 µs (Figure 6d) signifies that the TADF and the DF in the films of **2Cz2TAZ** are very fast (faster than 80 µs), suggesting strong competition with IC, in turn indicating that the aggregation itself in the films of this compound is beneficial and not detrimental to the TADF.

Based on these photophysical properties, we can reasonably consider **2Cz2TAZ** as a good host material, exhibiting high lowest triplet energy and fast triplet harvesting through TADF occurring between high-energy triples and S5. This is in addition to the suitable energy levels and high thermal stability demonstrated. However, in order to be utilized as a host material, **2Cz2TAZ** should possess appropriate charge transport properties, which is the focus of the next section.

2.6. Charge Transporting Properties

The charge transporting properties of **2Cz2TAZ** were studied at room temperature by the time-of-flight (TOF) technique (**Figure 7**) on samples with the structure of ITO/**2Cz2TAZ** film/Al. Aiming to investigate the effect of film-deposition conditions on charge-transporting properties of **2Cz2TAZ**, the films were deposited by thermal evaporation using low- and high deposition rates of ca. 3.7 and 10.7 Å s^{-1}, and are reported hereafter as LR- and HR films, respectively. The emission colors of the TOF samples with LR and HR films shown in the insets of Figure 7 are in line with the observed blueshifts of PL bands of LR and HR films of **2Cz2TAZ** shown in Figure S7 (Supporting Information) (see also Annex S3, Supporting Information).

By using the values of transient time (t_{tr}) fixed at the different electric fields, the thickness (d) of the deposited layer measured by ProFilm 3D (Figure S8a,b, Supporting Information), and the applied voltage (U), the hole and electron mobilities (μ_μ and μ_e) of **2Cz2TAZ** were calculated using the equation $\mu_{h/e} = d^2/(U \times t_{tr})$. Despite the dispersive hole and electron transport of **2Cz2TAZ**, the values of transient time (t_{tr}) were estimated when the TOF signals were plotted in log-log scales (Figure S8c,d, Supporting Information). These TOF signals confirm the presence of bipolar transport in LR and HR films. Charge extraction by linearly increasing voltage (CELIV) measurements additionally supports electron transport in the HR film (Figure S8e, Supporting Information).

The electric field dependencies of the hole mobility of the compound **2Cz2TAZ** at room temperature were additionally analyzed by the Poole-Frenkel relationship ($\mu_{hole} = \mu_0\, e^{\beta E 1/2}$), as shown in Figure 7. In this equation, μ_0 is zero-field mobility, β is the field dependence parameter, and E is the applied electric field. The obtained data are compiled in Table 1. The hole and electron mobility values were found to be different for LR and HR films of **2Cz2TAZ**. At the electric field of 1×10^6 V cm^{-1}, the LR film of **2Cz2TAZ** was characterized by more balanced mobility values in comparison to that of the HR film (Figure 7). The hole mobility values of LR and HR films of **2Cz2TAZ** were found to be of 4.1×10^{-5} and 3.1×10^{-5} cm^2 Vs^{-1} respectively at the electric field of 1×10^6 V cm^{-1}. The electron mobility values of LR and HR films of **2Cz2TAZ** were determined to be 1×10^{-4} and 2.1×10^{-4} cm^2 Vs^{-1}, respectively at the same electric field, which are slightly higher than the hole mobilities. Nevertheless, both the LR and HR films exhibit balanced bipolar hole and electron transport throughout of the selected electric field range, which is a desired property for a good host material.

2.7. Electroluminescence

Having determined that **2Cz2TAZ** is a promising host material due to its balanced bipolar charge mobility, triplet harvesting properties, suitable energy levels and high thermal stability, the electroluminescence of OLEDs containing **2Cz2TAZ** as host material in the emissive layer were studied. Aiming at estimating the efficiency of exciton production (χ), host-free OLEDs were first prepared using **2Cz2TAZ** as an emitter, with the structure ITO/HAT-CN (10 nm)/TAPC (40 nm)/TCTA (15 nm)/2Cz2TAZ (25 nm)/TSPO1 (4 nm)/TPBi (40 nm)/LiF (1.5 nm)/Al (+100 nm). (Figure S8, Supporting Information). A very small experimental maximum EQE of 1.3 % was obtained (Figure S9, Supporting Information), which is expected if we consider the deceiving PLQY of only 1.51–2.25% found for the THF and toluene solutions. Indeed, by utilizing the formula $\mu_{ext} = \gamma \times \phi_{PL} \times \chi \times \mu_{out}$, and by considering the highest PLQY of 4.67 % and the best- or typical values for the other parameters (χ of 100 %, outcoupling efficiency (μ_{out}) of 30 %, and the charge-balance factor (γ) of 100%), we can expect a maximum theoretical EQE of such OLEDs of 1.4%. The agreement between the experimental and the theoretical EQE values proves the validity of the assumed values for the parameters γ, χ, and μ_{out}, thus confirming the efficient triplet harvesting (χ~100%) and the balanced hole-electron transport (γ~100%) in light-emitting film of **2Cz2TAZ**.

However, the low PLQY value of the films limits the application of **2Cz2TAZ** as OLED emitter. Consequently, we utilized **2Cz2TAZ** as OLED host based on the excellent χ value of *ca.*100% because of the TADF and γ of *ca.*100% because of the bipolar charge transport.

To explore the performance of **2Cz2TAZ** as the OLED host, electroluminescent devices with the configuration ITO/HAT-CN (10 nm)/TAPC (40 nm)/TCTA (15 nm)/EML (emitter (15 wt.%):**2Cz2TAZ** (25 nm)/TSPO1 (4 nm)/TPBi (40 nm)/LiF (0.3 nm)/Al(100 nm) were fabricated. The TADF emitter 4CzTPN-Ph and phosphorescent emitter $Ir(Piq)_2(acac)$ emitters were

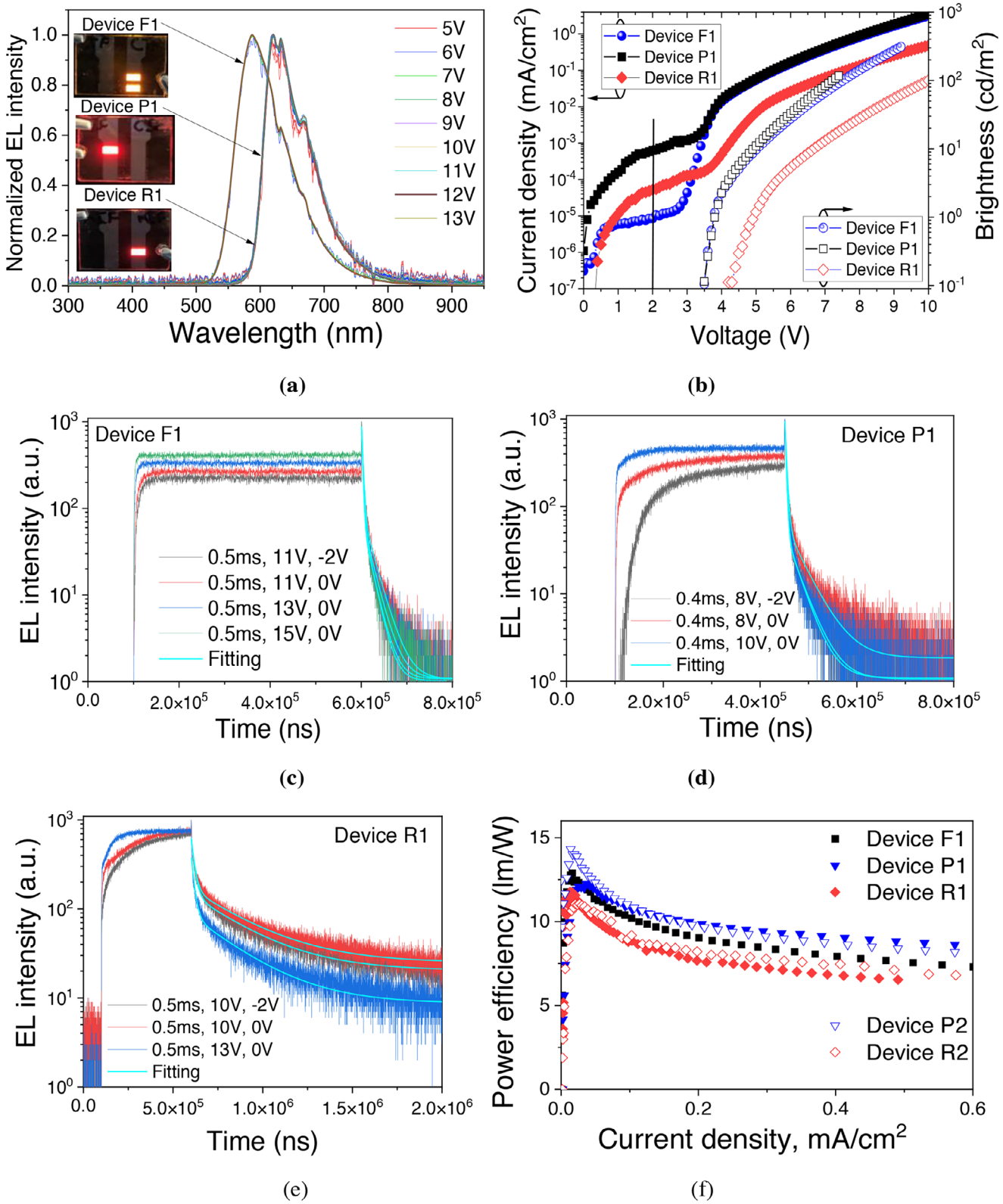

Figure 8. a) Normalized EL spectra recorded at different voltages; b) current density and luminescence versus voltage; EL responses at wavelengths of the maxima of EL spectra (parameters of the pulses are marked as follows pulse duration (τ_{pulse})/amplitude (V_{pulse})/voltage onset (V_{onset})) for devices c) F1, d) P1, e) R1 and f) the plots of power efficiency versus current density of the different devices.

selected for the fabrication of fluorescent and phosphorescent devices F1 and P1, respectively. In addition, the reference device R1 with commercial host mCBP for $Ir(Piq)_2(acac)$[15 wt.%] was fabricated using the same device structure. The equilibrium energy diagrams of the devices are demonstrated in Figure S10a,b (Supporting Information). The molecular structures of the materials used for the deposition of other functional layers are shown in Figure S10c (Supporting Information). Four pixels of each device were tested (see section "Electroluminescence" of the Supporting information (Figures S11–S13, Supporting Information)).

The electroluminescence (EL) spectra of devices F1, P1, and R1 are fully attributed to the emissions of the emitters, indicating complete host-guest energy transfer (**Figure 8**a). The EL spectra of the devices are very similar to the PL spectra of the layers of the corresponding emitters (Figure S14, Supporting Information). No changes were observed in the EL spectra in broad range of voltages for all the devices, demonstrating excellent chromaticity (Figure S15, Supporting Information). The CIE coordinates of (0.55, 0.43) of device F, (0.67, 0.32) of device P, and (0.67, 0.32) of device R1 correspond to red electroluminescence (Figure S15, Supporting Information). The CIE coordinates of $Ir(Piq)_2(acac)$-based devices are close to the reported ones.[39] Complete energy transfer from host **2Cz2TAZ** to emitters 4CzTPN-Ph or $Ir(Piq)_2(acac)$ takes place in the devices because the emission of the host is not observed.

Devices F1 and P1 containing host **2Cz2TAZ** were characterized by slightly lower turn-on voltages of 3.49 V compared to that of the reference device R1 based on the commercial host mCBP (3.89 V) (Figure 8b). Low turn-on voltages suggest an appropriate OLED structure with low charge barriers, indicating better performance of **2Cz2TAZ** as host material compared to the reference one (mCBP). The difference can be explained by the different energy barriers for the injection of holes to the light-emitting layers due to the different HOMO levels of **2Cz2TAZ** (−5.5 eV) and mCBP (−6.0 eV) (Figure S10a,b, Supporting Information). Devices F1 and P1 showed similar current densities at the voltages higher than the turn-on voltages. This observation indicates that the effect of different emitters on the charge-transporting properties of the devices is negligible. At the same voltages, device R1 showed lower current densities than devices F1 and P1. After the comparison, it was observed that **2Cz2TAZ** had better charge-transporting properties compared to mCBP, while those of all the other device layers remained the same. Device F1 showed very low dark current densities at voltages lower than the turn-on voltage of 3.49 V. For example, a dark current density of 1×10^{-5} mA cm^{-2} was observed for device F1 at 2 V. Such low dark current density can be attributed to the low charge leakages of device F1. This observation is supported by the results of analysis of EL decay curves (Figure 8c). Device F practically immediately showed the maximum EL intensity at the voltage onset (see the front site of the EL responses). In contrast, the maximum EL intensity was observed after more than 100 µs for $Ir(Piq)_2(acac)$-based devices P1 and R1 (Figure 8d,e). This means that the hole-electron balance cannot be easily reached apparently because of the very different hole and electron mobility values of the $Ir(Piq)_2(acac)$-containing light-emitting layers. This observation is in good agreement with the relatively high dark current densities of 7×10^{-4} and 4×10^{-4} mA cm^{-2} of devices P1 and R1, respectively estimated at 2 V.

Table 2. Electroluminescent parameters of the devices.

Device	λ_{EL} [a] [nm]	V_{on} [b] [V]	PE_{max} [c] [lm/W]	CE_{max} [d] [cd/A]	EQE_{max} [e] [%]
F1	589	3.49	12.89	18.20	8.1
P1	620	3.49	12.26	20.31	24.4
R1	620	3.89	11.76	21.46	26.09
P2	620	3.39	14.31	19.83	22.72
R2	620	3.89	11.06	19.11	18.14
P3	620	3.1	16.4	25	26.2
QW3	619	4.49	1.17	3.21	1.35
QW5	619	3.49	2.75	2.71	1.6

[a] Wavelength of electroluminescence. [b] Turn-on voltage at 1 cd/m^2. [c] Maximum power efficiency. [d] Maximum current efficiency. [e] Maximum external quantum efficiency.

The EL decay curves for devices F1, P1, and R1 were obtained in the microsecond range after the voltage was turned off (Figure 8c–e). The EL lifetimes of devices F1 (11.6 µs at V_{pulse} of 11 V) and P1 (10.7 µs at V_{pulse} of 10 V) were more than ten times faster in comparison to that of the reference device R1 (249.6 µs at V_{pulse} of 10 V) (Table S7, Supporting Information).

The same trend was observed for the devices (F2 and P2) containing the layers of 10 wt.% solid solutions of 4CzTPN-Ph or 10 wt.% of $Ir(Piq)_2(acac)$ in **2Cz2TAZ** or mCBP as emitting layers (Figure S16, Supporting Information). This observation indicates that the host **2Cz2TAZ** enables significantly faster electroluminescence compared to the host mCBP when using the $Ir(Piq)_2(acac)$ emitter. This additional OLED with the emitting layer of the blend of $Ir(Piq)_2(acac)$ [10 wt.%] and **2Cz2TAZ** (P2) exhibited a higher maximum EQE than the reference device with the emitting layer of $Ir(Piq)_2(acac)$ [10 wt.%] in mCBP (R2) (**Table 2**). The rapid decay of electroluminescence using **2Cz2TAZ** as host can be related to its fast TADF and balanced charge-transporting properties (Figure 7). Conventional intramolecular CT-based TADF emitters typically exhibit delayed fluorescence with the lifetimes in the range of microseconds to milliseconds.[40,41] In contrast, **2Cz2TAZ** showed TADF with the lifetimes in the range of nanoseconds (Figure 6b). As a result, **2Cz2TAZ** allowed fast triplet harvesting and rapid energy transfer to the emitters leading to lower efficiency roll-offs (Figure 8f). Because of the short EL lifetimes (Figure 8c–e), **2Cz2TAZ** helps reduce second-order annihilation processes, such as triplet–triplet annihilation (TTA) and triplet–polaron quenching (TPQ), thereby minimizing efficiency roll-off and enhancing device lifetime.[42]

The maximum EQE values of 4CzTPN-Ph-based device F1 (8.1%) and $Ir(Piq)_2(acac)$-based device P1 (24.4%) are in good agreement with those of previously published devices (Table 2).[28,43] For example, a commercialized host used for 4CzTPN-Ph allowed to obtain the maximum EQE of 7.7%.[43] 4CzTPN-Ph-based TADF OLEDs showed maximum EQE of 11.2%.[28] Notably, device P3 showed the higher EQE of 26.2 % compared to device P2 after additional optimization of the thickness of the light-emitting layer (Table 2; and Figure S17, Supporting Information). The **2Cz2TAZ**-based devices demonstrated significantly superior performance compared to the first reported red phosphorescent $Ir(Piq)_2(acac)$-based OLEDs with V_{on} and

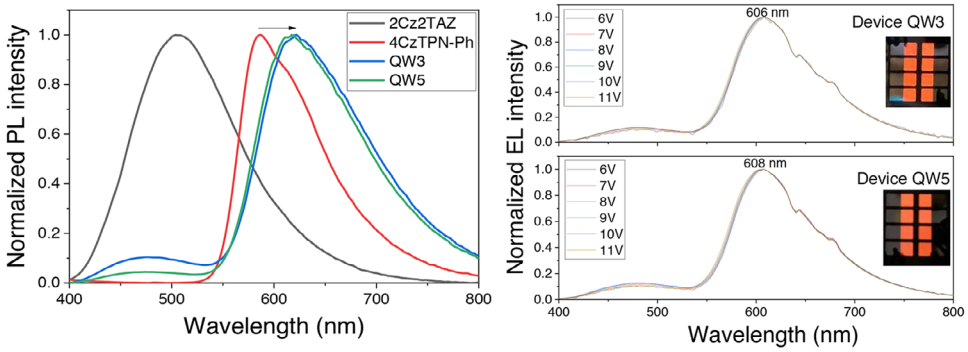

Figure 9. a) PL and b) EL spectra of (a) host-free films and (b) wells-based devices QW3 and QW5.

EQE values of 8.53 V and 8.46 %.[44] Additionally, the maximum EQE of 6.13% was obtained for $Ir(Piq)_2(acac)$-based devices with the similar device structure to that of device P.[45] Nowadays, red $Ir(Piq)_2(acac)$-based phosphorescent OLEDs are characterized by maximum EQEs that slightly exceed 20%.[46] Taking into account the above analysis, it can be stated that the newly synthesized compound **2Cz2TAZ** exhibits very promising performance as a host. Predictively, the usage of **2Cz2TAZ** as a host material is not limited to the tested red emitters. It can be recommended for green or even blue emitters considering recently proposed sensitization processes in TADF OLEDs.[47]

Hosting properties of **2Cz2TAZ** were additionally studied using the multilayer exciton-confinement architecture, analogous to a quantum well structure approach.[48,49] The host **2Cz2TAZ** allowed us to shift the PL spectrum of the neat film of TADF emitter 4CzTPN-Ph peaking at 589 nm to the red region (**Figure** 9a). The analysis of PL spectra of the light-emitting layers and the EL spectra of devices QW3 and QW5 (Figure 9a,b) shows that residual emission in the 400–525 nm range was observed under both optical and electrical excitation. This comparison of PL and EL spectra indicates that the emission band at the wavelengths of 400–525 nm stems from the host **2Cz2TAZ**. The presence of the **2Cz2TAZ** emission band suggests incomplete host-guest energy transfer (Figure S18, Supporting Information). This spectral data aligns with those of previously developed QW-based OLEDs.[50] Notably, as the periodicity of the double layers containing host **2Cz2TAZ** and emitter 4CzTPN-Ph increases from three (QW3) to five (QW5), the intensity of the emission band at 400–525 nm decreases. Therefore, the further increase of the periodicity in the light-emitting layers could lead to complete host-guest energy transfer. The 30 nm thick films of QW3 ((4CzTPN-Ph/**2Cz2TAZ**)$_3$ (5 nm/3 nm) and QW5 ((4CzTPN-Ph/**2Cz2TAZ**)$_5$ (4 nm/1.2 nm)) with different periodicities (3 and 5, respectively) of **2Cz2TAZ** and 4CzTPN-Ph showed PL spectra centered at 619 nm. The corresponding QW3 and QW5 devices showed red electroluminescence and EQEs of 1.35 and 1.6 %, respectively (Table 2; Figures S19 and S20, Supporting Information). These EQE values of devices QW3 and QW5 are lower than EQE of device F1 (8.1%) based on guest-host light-emitting layer of 4CzTPN-Ph and **2Cz2TAZ**. However, devices QW3 and QW5 demonstrated deep-red electroluminescence with color coordinates of (0.58, 0.41) (Figure 9b).

3. Conclusion

We report on the newly designed carbazole and triazine derivative that was synthesized by a Suzuki cross-coupling reaction in the high yield of 82%. After theoretical and experimental investigations, it is demonstrated that this compound has good hosting properties for red emitters, and promising hosting properties for green or blue emitters. The films of this compound show ionization energy of 5.5 eV and electron affinity of 2.33 eV. Hole mobilities of the differently prepared films range from 3.1×10^{-5} to 4.1×10^{-5} cm^2 Vs^{-1}, and the electron mobilities range from 1×10^{-4} to 2.1×10^{-4} cm^2 Vs^{-1} at the electric field of 1×10^6 V/cm. The vacuum-deposited films of the compound show combination of prompt and delayed fluoresce. Thermally activated delayed fluorescence has an average lifetime of 79 ns. Red fluorescent and phosphorescent organic light-emitting diodes fabricated using the newly synthesized compound as a host show relatively high external quantum efficiencies of 8.1 and 26.2%, respectively. In comparison to the devices with the conventional host mCBP, devices prepared using the newly synthesized host have shortened average electroluminescence lifetimes of 10.7 µs. The control device with the same structure but with the conventional host shows the average lifetime of electroluminescence of 249.6 µs. The shortened electroluminescent lifetime leads to an improvement in the efficiency roll-off of the fluorescent and phosphorescent organic light-emitting diodes due to the perfect hole-electron balance and fast triplet harvesting offered by the newly developed host.

4. Experimental Section

Computational Details: Ground-state geometries for **2Cz2TAZ** were optimized at the DFT/ LC-*ωPBEh level theory in conjunction with the def2-SVP basis set, and the polarizable continuum model with a dielectric constant of 2.38 corresponding to the toluene. The golden ratio algorithm was employed to tune the ω-parameter values for the range-separated hybrid LC-*ωPBEh functional using Terachem 1.96. The optimally tuned ω value in toluene for LC-*ωPBEh is 0.0518 $Bohr^{-1}$, which was significantly smaller than the default value of 0.200 $Bohr^{-1}$. The RISC reorganization energy, accounting for implicit solvent using the COSMO model was obtained using NWCHEM at the same functional and tuned *ω. SOC was obtained using ORCA 5.04 using ω*B97XD/def-2svp. LC-ω*pbeh/def-2svp and ω*B97XD/def-2svp yield very similar results in terms of energy level (Table S1, Supporting Information). SOC between singlets and triplets

was calculated on S0 optimized geometries from TD-DFT by using quasi-degenerate perturbation theory without Tamm–Dancoff approximation as implemented by de Souza et al.[51]

The π–π stacked structures were extracted from molecular dynamic simulation performed using the GROMACS 2021.2 with topologies generated using the Automated Topology Builder 3.0. Temperature coupling was achieved using the V-rescale method with a stochastic term and a time constant of 1 ps to maintain the system temperature. In the NPT ensemble, a Parrinello-Rahman coupling with a time constant of 5 ps was employed. The LINCS algorithm was used to constrain all bond lengths within the system with non-bonded interactions within a 1.4 nm cutoff were evaluated at each step using particle mesh Ewald (PME) for long-range Coulomb interactions.

Materials: The synthesis procedures and identification of **2Cz2TAZ** is described in detail in the Supporting Information.

All OLED functional materials were purchased from commercial suppliers Sigma-Aldrich or Lumtec. Dipyrazino[2,3-f:2′,3′-h]quinoxaline-2,3,6,7,10,11-hexacarbonitrile (HAT-CN), 4,4′-cyclohexylidenebis[N,N-bis(4-methylphenyl)benzenamine] (TAPC), tris(4-carbazoyl-9-ylphenyl)amine (TCTA). 3,3-Di(9*H*-carbazol-9-yl)biphenyl (mCBP), 2,3,5,6-tetrakis(3,6-diphenylcarbazol-9-yl)-1,4-dicyanobenzene (4CzTPN-Ph), bis(1-phenylisoquinoline)(acetylacetonate)iridium(III) ($Ir(piq)_2(acac)$), diphenyl[4-(triphenylsilyl)phenyl]phosphine oxide (TSPO1), 2,2′,2′′-(1,3,5-benzinetriyl)-tris(1-phenyl-1-H-benzimidazole) (TPBi), and lithium fluoride (LiF) were used as received without further purification.

Supporting Information

Supporting Information is available from the Wiley Online Library or from the author.

Acknowledgements

This project has received funding from the Research Council of Lithuania, project QUANT, agreement no S-LU-24-8.

Conflict of Interest

The authors declare no conflict of interest.

Data Availability Statement

The data that support the findings of this study are available in the supplementary material of this article.

Keywords

bipolar charge-transport, organic light-emitting diodes, tunability

Received: June 6, 2025
Revised: August 8, 2025
Published online: September 18, 2025

[1] C. W. Tang, S. A. VanSlyke, *Appl. Phys. Lett.* **1987**, *51*, 913.
[2] S. Wang, Y. Sun, Z. Wu, Y. Liu, L. Zhao, S. Li, X. Dong, W. Wang, *Dyes Pigm.* **2023**, *220*, 111578.
[3] G. Hong, X. Gan, C. Leonhardt, Z. Zhang, J. Seibert, J. M. Busch, S. Bräse, *Adv. Mater.* **2021**, *33*, 9.
[4] J. Wang, F. Zhang, J. Zhang, W. Tang, A. Tang, H. Peng, Z. Xu, F. Teng, Y. Wang, *J. Photochem. Photobiol. C: Photochem. Rev.* **2013**, *17*, 69.
[5] Y. Gawale, R. Ansari, K. R. Naveen, J. H. Kwon, *Front. Chem.* **2023**, *11*, 1211345.
[6] J. Jayabharathi, V. Thanikachalam, S. Thilagavathy, *Coord. Chem. Rev.* **2023**, *483*, 215100.
[7] M. Sarma, L. M. Chen, Y. S. Chen, K. T. Wong, *Mater. Sci. Eng. R Rep.* **2022**, *150*, 100689.
[8] L. Xiao, Z. Chen, B. Qu, J. Luo, S. Kong, Q. Gong, J. Kido, *Adv. Mater.* **2011**, *23*, 926.
[9] K. Thakur, B. van der Zee, G.-J. A. H. Wetzelaer, C. Ramanan, P W. M Blom, *Adv. Opt. Mater.* **2022**, *10*, 2101784.
[10] Z. Ma, W. Dong, X. Lü, P. Chen, J. Hou, Q. Duan, S. Shao, *Dyes Pigm.* **2020**, *174*, 108097.
[11] C. Liu, T. Li, M. Sun, M. Xie, Y. Zhou, W. Feng, Q. Sun, S. T. Zhang, S. Xue, W. Yang, *Adv. Funct. Mater.* **2023**, *33*, 26.
[12] T. Chatterjee, K. T. Wong, *Adv. Opt. Mater.* **2019**, *7*, 1800565.
[13] X. Cai, R. Liu, H. Shi, C. Li, H. Zhu, *Dyes Pigm.* **2017**, *143*, 196.
[14] H. J. Jang, R. Braveenth, K. Raagulan, S Yu Choi, Y. H. Park, Su B Oh, Il-Ji Bae, Bo Mi Kim, Q. Wu, M. Kim, K. Y. Chai, *Dyes Pigm.* **2020**, *182*, 108697.
[15] P. Kautny, Z. Wu, J. Eichelter, E. Horkel, B. Stöger, J. Chen, D. Ma, J. Fröhlich, D. Lumpi, *Org. Electron.* **2016**, *34*, 237.
[16] B. Wex, B. R. Kaafarani, *J. Mater. Chem. C. Mater.* **2017**, *5*, 34.
[17] Z. B Cai, L. J. Chen, S. L. Li, Q. Ye, Y. P Tian, *Dyes Pigm.* **2020**, *175*, 108115.
[18] W. Qu, Z. Gao, W. Li, X. Fan, Y. Shi, Y. Miao, G. Yu, H. Zhou, J. Huang, H. Wang, *Dyes Pigm.* **2021**, *196*, 109808.
[19] E. Celik, M. Guzel, S. O. Kart, M. Ak, H. H. Kart, *J. Mol. Struct.* **2024**, *1299*, 137198.
[20] G. Zhang, A. M. Elewa, M. Rashad, S. Helali, H. H. Chou, A. F. M. EL-Mahdy, *Microporous Mesoporous Mater.* **2024**, *363*, 112824.
[21] L. Bao, J. Zhu, W. Song, H. Zhou, J. Huang, H. Mu, J. Su, *Org. Electron.* **2020**, *83*, 105672.
[22] Y. Hasegawa, Y. Yamada, M. Sasaki, T. Hosokai, H. Nakanotani, C. Adachi, *J. Phys. Chem. Lett.* **2018**, *9*, 863.
[23] J. W. Sun, J.-H. Lee, C.-K. Moon, K. H. Kim, H. Shin, J. J. Kim, *Adv. Mater.* **2014**, *26*, 32.
[24] K. H. Kim, J. J. Kim, *Adv. Mater.* **2018**, *30*, 42.
[25] F. Tenopala-Carmona, O S. Lee, E. Crovini, A M. Neferu, C. Murawski, Y. Olivier, E. Zysman-Colman, M C. Gather, *Adv. Mater.* **2021**, *33*, 37.
[26] Q. Zhang, S. Guo, K. Zhang, C. Yu, H. Zhou, Q. Wang, Z. Zhang, J. Huang, H. Wang, B. Wei, *Dyes Pigm.* **2024**, *222*, 111874.
[27] W. Luo, T. T. Wang, X. Chen, K. N. Tong, W. He, S. Q. Sun, Y. J. Zhang, L. S. Liao, M. K. Fung, *J. Mater. Chem. C Mater.* **2020**, *8*, 30.
[28] H. Uoyama, K. Goushi, K. Shizu, H. Nomura, C. Adachi, *Nature* **2012**, *492*, 234.
[29] R. Skaisgiris, T. Serevičius, J. Dodonova, D. Banevičius, K. Kazlauskas, S. Tumkevičius, S. Juršėnas, *J. Lumin.* **2022**, *241*, 118473.
[30] S. Kuila, H. Miranda-Salinas, J. Eng, C. Li, M. R. Bryce, T. J. Penfold, A. P. Monkman, *Nat. Commun.* **2024**, *15*, 9611.
[31] P. Data, M. Okazaki, S. Minakata, Y. Takeda, *J. Mater. Chem. C Mater.* **2019**, *7*, 6616.
[32] M. Okazaki, Y. Takeda, P. Data, P. Pander, H. Higginbotham, A. P. Monkman, S. Minakata, *Chem. Sci.* **2017**, *8*, 2677.
[33] M. Kasha, *Discuss. Faraday. Soc.* **1950**, *9*, 14.
[34] T. Zhang, Y. Xiao, H. Wang, S. Kong, R. Huang, V. Ka-Man Au, T. Yu, W. Huang, *Angew. Chem., Int. Ed.* **2023**, *62*, 39.
[35] A. A. Rudnick, S. Bagnich, D. Wagner, S. Athanasopolous, P. Strohriegl, A. Köhler, *J. Chem. Phys.* **2016**, *144*, 21.
[36] G. K. Belousov, A. A. Vaitusionak, I. V. Vasilenko, M. Ghasemi, V. Andruleviciene, A. Ivanchanka, D. Volyniuk, H. Kim, J. V. Grazulevicius, S. V. Kostjuk, *Macromolecules* **2023**, *56*, 2686.

[37] Y. Danyliv, K. Ivaniuk, I. Danyliv, O. Bezvikonnyi, D. Volyniuk, S. Galyna, A. Lazauskas, L. Skhirtladze, H. Ågren, P. Stakhira, N. Karaush-Karmazin, A. Ali, G. Baryshnikov, J. V. Grazulevicius, *Dyes Pigm.* **2023**, *208*, 110841.
[38] H. Wu, Y. Zhang, M. Zhao, X. Jin, H. Zhou, Y. Miao, Y. Huang, J. Huang, H. Wang, J. Su, *Dyes Pigm.* **2022**, 207.
[39] P. Arsenyan, A. Petrenko, K. Leitonas, D. Volyniuk, J. Simokaitiene, T. Klinavicius, E. Skuodis, J.-H. Lee, J. V. Grazulevicius, *Inorg. Chem.* **2019**, *58*, 10174.
[40] X. Hong, D. Zhang, C. Yin, Qi Wang, Y. Zhang, T. Huang, J. Wei, X. Zeng, G. Meng, X. Wang, G. Li, D. Yang, D. Ma, L. Duan, *Chem* **2022**, *8*, 1705.
[41] P. Jiang, J. Miao, X. Cao, H. Xia, K. Pan, T. Hua, X. Lv, Z. Huang, Y. Zou, C. Yang, *Adv. Mater.* **2022**, *34*, 3.
[42] M. Greenberg, S. Sanderson, R. D. White, G. Vamvounis, P. L. Burn, B. Philippa, *J. Chem. Phys.* **2023**, *159*, 3.
[43] Z. Liu, Y. Lei, C. Fan, X. Peng, X. Ji, G. E. Jabbour, X. Yang, *Org. Electron.* **2017**, *41*, 237.
[44] Y.-J. Su, H.-L. Huang, C.-L. Li, C.-H. Chien, Y.-T. Tao, P.-T. Chou, S. Datta, R.-S. Liu, *Adv. Mater.* **2003**, *15*, 884.
[45] Z. Chen, H. Zhang, D. Wen, W. Wu, Q. Zeng, S. Chen, W. Y. Wong, *Chem. Sci.* **2020**, *11*, 9.
[46] C.-H. Fan, P. Sun, T.-H. Su, C.-H. Cheng, *Adv. Mater.* **2011**, *23*, 2981.
[47] K. Stavrou, L. G. Franca, A. Danos, A. P. Monkman, *Nat. Photonics* **2024**, *18*, 554.
[48] I. G. Jang, V. Murugadoss, T. H. Park, K. R. Son, H. J. Lee, W. Q. Ren, M. J. Yu, T. G. Kim, *Nanomicro Lett.* **2022**, *14*, 60.
[49] S. H. Yang, B. C. Hong, S. F. Huang, *J. Appl. Phys.* **2009**, *105*, 113105.
[50] L. Meng, H. Wang, X. Wei, J. Liu, Y. Chen, X. Kong, X. Lv, P. Wang, Y. Wang, *ACS Appl. Mater. Interfaces* **2016**, *8*, 20955.
[51] B. De Souza, G. Farias, F. Neese, R. Izsák, *J. Chem. Theory. Comput.* **2019**, *15*, 1896.